Successive bifurcations in a fully three-dimensional open cavity flow

F. Picella[1], **J.-Ch. Loiseau**[1], **F. Lusseyran**[2], **J.-Ch. Robinet**[1,†], **S. Cherubini**[3] **and L. Pastur**[4]

[1]DynFluid – Arts et Métiers ParisTech, 151 Bd. de l'Hôpital, 75013 Paris, France

[2]LIMSI, CNRS, Université Paris-Saclay, Bat. 508, Rue John Von Neumann, Campus Universitaire, 91403 Orsay, France

[3]DMMM, Politecnico di Bari, Via Re David 200, 70126 Bari, Italy

[4]LIMSI, CNRS, Université Paris-Sud, Université Paris-Saclay, Bat. 508, Rue John Von Neumann, 91403 Orsay, France

The transition to unsteadiness of a three-dimensional open cavity flow is investigated using the joint application of direct numerical simulations and fully three-dimensional linear stability analyses, providing a clear understanding of the first two bifurcations occurring in the flow. The first bifurcation is characterized by the emergence of Taylor–Görtler-like vortices resulting from a centrifugal instability of the primary vortex core. Further increasing the Reynolds number eventually triggers self-sustained periodic oscillations of the flow in the vicinity of the spanwise end walls of the cavity. This secondary instability causes the emergence of a new set of Taylor–Görtler vortices experiencing a spanwise drift directed toward the spanwise end walls of the cavity. While a two-dimensional stability analysis would fail to capture this secondary instability due to the neglect of the lateral walls, it is the first time to our knowledge that this drifting of the vortices can be entirely characterized by a three-dimensional linear stability analysis of the flow. Good agreements with experimental observations and measurements strongly support our claim that the initial stages of the transition to turbulence of three-dimensional open cavity flows are solely governed by modal instabilities.

Key words: bifurcation, instability, nonlinear dynamical systems

---

1. Introduction

Centrifugal forces are ubiquitous in nature and can have a tremendous impact on a large variety of physical systems, ranging from astrophysical objects to man-made experimental devices. Typical examples are accretion disks and planetary cores (Gurnett *et al.* 2007) where centrifugal forces can cause an instability of the system giving rise to spatial patterns strongly affecting its dynamics (Sisan *et al.* 2004). At human scale, these centrifugal forces can be found in granular or stratified flows

† Email address for correspondence: jean-christophe.robinet@ensam.eu

between concentric cylinders (Molemaker, McWilliams & Yavneh 2001; Conway, Shinbrot & Glasser 2004), in separated boundary layer flows (Theofilis, Hein & Dallmann 2000; Cherubini *et al.* 2010) as well as in a number of confined flows such as the flow within a lid-driven cavity (Ramanan & Homsy 1994; Albensoeder, Kuhlmann & Rath 2001; Theofilis *et al.* 2004). In all cases, if the underlying unstable equilibrium is a two-dimensional flow, centrifugal instabilities trigger a three-dimensionalization of this flow. One of the first striking observations of these three-dimensional centrifugal patterns was reported by Denham & Patrick (1974) for the flow over a backward-facing step. This behaviour was later explained by a stability analysis conducted on a spanwise-homogeneous two-dimensional base flow, as reported in Barkley, Gomes & Henderson (2002). In such a flow, the primary instability has the form of flat rolls, eventually saturating into counter-rotating elongated vortical structures, the so-called Taylor–Görtler vortices (Beaudoin *et al.* 2004).

The flow investigated in the present work is the incompressible open cavity flow, also known as the shear-driven cavity flow. It is a geometrically induced separated boundary layer flow having a number of applications in aeronautics. Based on the assumption of two-dimensionality, it has been shown that the leading two-dimensional instability of this flow is mostly localized along the shear layer developing at the interface between the outer boundary layer flow and the inner cavity flow (Sipp *et al.* 2010). This oscillatory global instability of the external shear layer relies on two essential mechanisms: the convectively unstable nature of the shear layer which causes perturbations to grow as they travel downstream, and the instantaneous pressure feedback when the perturbation impacts the downstream corner of the cavity, allowing these same perturbations to eventually re-excite the upstream shear layer and hence giving rise to a linearly unstable feedback loop at sufficiently high Reynolds numbers. For compressible shear-driven cavity flows, a similar unstable feedback loop exists wherein the feedback is given by upstream-propagating acoustic waves (Rossiter 1964; Rowley, Colonius & Basu 2002; Yamouni, Sipp & Jacquin 2013). This strictly two-dimensional linearly unstable flow configuration has served multiple purposes over the past decade: illustration of optimal control and reduced-order modelling (Barbagallo, Sipp & Schmid 2009), investigation of the nonlinear saturation process of globally unstable flows (Sipp & Lebedev 2007) and introduction to dynamic modes decomposition (Schmid 2010) to name just a few.

Considering strictly two-dimensional perturbations on top of this already two-dimensional base flow is however quite often an over-idealization of the problem. In order to circumvent this drawback, the perturbations are now considered as being spanwise periodic. This ansatz has proved necessary in order to capture the centrifugal instability experienced by the flow. Since the early work of Ramanan & Homsy (1994) on the stability of a two-dimensional lid-driven cavity toward spanwise-periodic perturbations, a large body of literature has been published wherein this ansatz enables the description of physical instabilities and mechanisms in qualitative agreement with necessarily three-dimensional experimental set-ups. For the lid-driven cavity flow, one can cite Ding & Kawahara (1998), Albensoeder *et al.* (2001), Guermond *et al.* (2002), Theofilis *et al.* (2004), Albensoeder & Kuhlmann (2006), Non, Pierre & Gervais (2006), Chicheportiche *et al.* (2008), while the reader is referred to the recent works of Meseguer-Garrido *et al.* (2014) and Citro *et al.* (2015*a*) and references therein for the shear-driven cavity flow.

Despite its qualitative success, linear stability analysis of a strictly two-dimensional base flow toward spanwise-periodic perturbations is still a relatively restrictive

hypothesis, real flows being rarely homogeneous in the spanwise direction. More often than not, flows studied experimentally necessarily have spanwise end walls whose influence cannot be accounted for with the previously cited approach. The existence of such spanwise end walls moreover gives rise to the formation of lateral boundary layers which can induce large-scale secondary motions, which in turn can influence the stability of the flow as demonstrated experimentally by Faure *et al.* (2007, 2009) and Douay, Pastur & Lusseyran (2016*b*). In order to take properly into account the influence of the spanwise end walls on the stability of the flow, these need to be included in the analysis. The linear stability analysis of a three-dimensional base flow toward three-dimensional perturbations is thus mandatory to obtain a realistic picture. Such fully three-dimensional stability analysis, however, is still a formidable computational task and very few references exist in the literature at this time. One can cite the original work of Bagheri *et al.* (2009*b*), Ilak *et al.* (2012) and Peplinski, Schlatter & Henningson (2015) on jets in cross-flow, or Loiseau *et al.* (2014) and Citro *et al.* (2015*b*) on roughness-induced transition in boundary layer flows. Feldman & Gelfgat (2010), Gómez, Gómez & Theofilis (2014), Kuhlmann & Albensoeder (2014) and Loiseau, Robinet & Leriche (2016) have also studied the three-dimensional linear stability of lid-driven cavity flows. To our knowledge, however, the body of literature existing on the instability and transition of realistic three-dimensional shear-driven cavities is essentially limited to Liu, Gómez & Theofilis (2016). These authors have reported a linear stability analysis of the flow over a long rectangular open cavity with a narrow span. Their key finding is that, for such long and narrow cavities, the transition to unsteadiness results from an instability of the shear layer reminiscent of the two-dimensional Rossiter modes.

Joining experimental observations, direct numerical simulations and fully three-dimensional linear stability analyses, the present work aims at shedding more light onto the initial stages of transition to unsteadiness of a realistic three-dimensional shear-driven cavity flow. Contrary to Liu *et al.* (2016), we consider herein a relatively large cavity whose aspect ratios are given by $L:D:S = 1:1:6$, where L, D and S are the streamwise length, the depth and the span of the cavity, respectively. Among other things, the results presented herein illustrate the importance of lateral walls to the stability of the flow. They particularly highlight how the spanwise drift of the Taylor–Görtler vortices, reported in a number of experimental studies (Faure *et al.* 2009; Douay *et al.* 2016*b*), is triggered by a secondary instability of the flow which cannot be captured using a traditional two-dimensional assumption of the base flow field. The extremely good agreement between the experimental observations and the predictions of linear stability analyses enables us to provide a simple scenario of the transition to unsteadiness experienced by the flow. The agreement between experimental evidence and theoretical predictions, moreover, strongly supports our claim that the initial stages of transition of the three-dimensional shear-driven cavity flow are solely governed by modal instabilities. The present manuscript is organized as follows. The experimental set-up is presented in § 2 while § 3 describes the numerical set-up and methods used. The fully three-dimensional linear stability analyses performed are presented in § 4. A thorough comparison of the numerical predictions and the experimental observations is given in § 5.1. Finally, § 6 presents our conclusions and some perspectives on this work.

2. Experimental set-up

Experiments reported in the present work were performed in the wind tunnel facility at LIMSI-Orsay (Faure *et al.* 2009; Basley *et al.* 2013, 2014; Douay *et al.* 2016*b*).
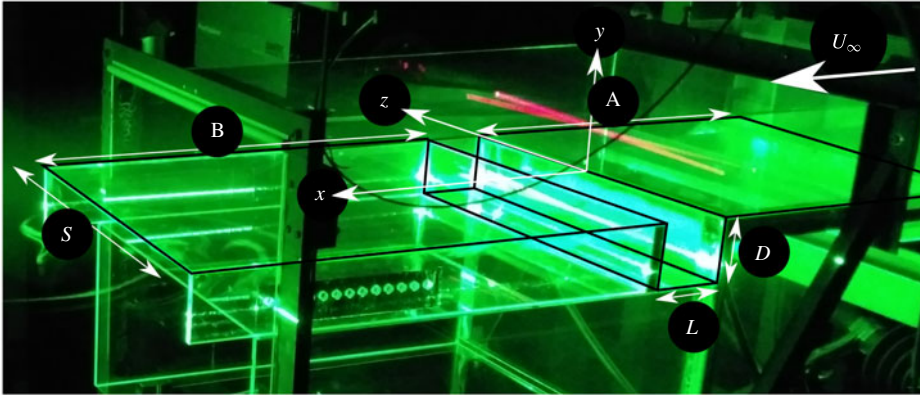
FIGURE 1. (Colour online) Picture of the experimental set-up at LIMSI (Orsay, France), as described by Faure *et al.* (2007).

The experimental set-up is shown in figure 1. The flow is made laminar by a calming section located downstream of the centrifugal fan: it is made of a settling chamber followed by a convergent and two honeycomb panels at the inlet of the contraction duct. The outlet of the wind tunnel is open to the room. The origin of the boundary layer is fixed by an elliptical leading edge, 300 mm upstream of the cavity leading edge, where a Blasius-like velocity profile develops. Background turbulence, estimated by laser Doppler velocimetry, is smaller than 1 %. The wind tunnel force frequencies were mainly distributed between 0 and 10 Hz, with a maximal power around 1 Hz, three orders of magnitude smaller than the cavity flow spectrum for the same frequency range. The span of the wind tunnel is $S = 300$ mm, while the top-to-bottom distance is 75 mm. The cavity depth is $D = 50$ mm. Centrifugal instabilities develop at very low incoming velocity, typically less than 1 m s^{-1}, which is challenging for the flow rate regulation. The incoming velocity stability is approximately 0.025 m s^{-1}, which also provides the lower limit of the velocity step. Complete optical access is made available using coated glass walls for the test section and the cavity. The cavity itself consists of three distinct rectangular elements, in coated glass. The first element is a forward-facing step at the inlet of the test section, much deeper than the cavity depth. The second element is the base floor which sets the cavity depth D. Finally, the last element is a D-deep forward-facing step which can slide above the flat floor of the second element, so as to adjust the cavity length L. As the flow is sensitive to inaccuracies in the cavity assembly, we had to pay particular attention to suppress any leak that could be present at the edges and corners of the cavity. In addition, the incoming flow has a very small, though non-vanishing, spanwise component, introducing a systematic bias in the incoming flow direction which is not strictly streamwise. Visualizations of the flow patterns presented later on are carried out by lighting up the smoke produced by a fog machine with a laser sheet generated by a 200 mJ Quantel twin-pulsed YAG laser. A standard, single-frame video camera (AVT Cameras, Marlin, 1024 pixel × 768 pixel of size 4.65 μm × 4.65 μm with resolution depth of 8 bit) snaps images at a frame rate of 20 Hz. An electronic delay generator (R&D Vision) is used to synchronize flash lamps and Q-switches of both laser cavities together with the camera's through the lens (TTL) signal.
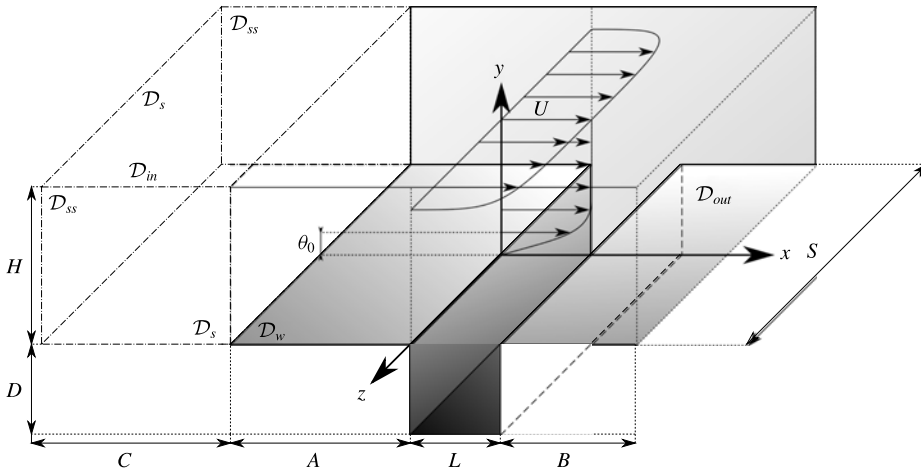
FIGURE 2. Sketch of a three-dimensional open cavity flow, showing the geometrical features. The shaded areas highlight the walls where no-slip boundary conditions are imposed.

3. Problem statement and numerical methods

3.1. *Governing equations*

The dynamics of the incompressible flow of a Newtonian fluid over an open cavity is governed by the Navier–Stokes equations

$$\frac{\partial \boldsymbol{u}}{\partial t} = -(\boldsymbol{u} \cdot \nabla)\boldsymbol{u} - \nabla p + \frac{1}{Re}\nabla^2 \boldsymbol{u}, \tag{3.1}$$

$$\nabla \cdot \boldsymbol{u} = 0, \tag{3.2}$$

where $\boldsymbol{u} = (u(\boldsymbol{x}, t), v(\boldsymbol{x}, t), w(\boldsymbol{x}, t))^{\mathrm{T}}$ is the velocity field and $p(\boldsymbol{x}, t)$ is the pressure field. The Reynolds number is defined as $Re = U_\infty L/\nu$, where U_∞ is the free-stream velocity, L is the length of the cavity and ν is the kinematic viscosity of the fluid. The reference frame $\boldsymbol{x} = (x, y, z)^{\mathrm{T}}$ is chosen such that x is the streamwise, y the wall-normal and z the spanwise direction. The flow configuration is sketched in figure 2, where the boundary conditions are indicated using the symbols listed in table 1. Following Sipp & Lebedev (2007) and Citro *et al.* (2015*a*), a fully three-dimensional boundary layer is obtained from a free-slip/no-slip discontinuity in the boundary condition.

The Navier–Stokes equations are solved using the incompressible flow solver NEK5000 (Fischer *et al.* 2008) which is based on the spectral element method (SEM). A $\mathbb{P}_N - \mathbb{P}_{N-2}$ formulation has been used: the velocity field is discretized using Nth degree Lagrange interpolants, defined on the Gauss–Legendre–Lobatto quadrature points, as basis and trial functions, while the pressure field is discretized using Lagrange interpolants of degree $N - 2$ defined on the Gauss–Legendre quadrature points. Finally, the time integration is performed using the BDF3/EXT3 scheme: integration of the viscous terms relies on the backward differentiation (BDF3), while the convective terms are integrated via extrapolation (EXT3), both methods being third-order accurate. The Navier–Stokes equations are discretized on a mesh of 30 000 spectral elements with polynomials of order 8. Thus, the problem to be solved consists of over 61 million degrees of freedom for describing the velocity and pressure fields.

Identifier	Description
$\mathcal{D}_{in}$	$(u, v, w) = (1, 0, 0)$
$\mathcal{D}_{s}$	$(\partial_y u, v, \partial_y w) = (0, 0, 0)$
$\mathcal{D}_{ss}$	$(\partial_z u, \partial_z v, w) = (0, 0, 0)$
$\mathcal{D}_{w}$	$(u, v, w) = (0, 0, 0)$
$\mathcal{D}_{out}$	$\left(p - \dfrac{1}{Re}\nabla u \right) \cdot n = 0$

TABLE 1. Description of the boundary conditions, with reference to figure 2.

3.2. *Linear stability analysis*

Steady solutions $Q(x) = (U_b, P_b)^{\mathrm{T}}$ to the Navier–Stokes equations are known as base flows or fixed points of the system. Their linear stability is dictated by the fate of infinitesimal perturbations evolving in their vicinity. The dynamics of such perturbations is governed by the linearized Navier–Stokes equations, which can be compactly written as

$$\frac{\partial u}{\partial t} = Ju \tag{3.3}$$

once projected onto a divergence-free vector space. As this linear dynamical system is autonomous in time, the perturbation u can be expanded into normal modes, such that $u(x, t) = \sum_{k=1}^{\infty} \hat{u}_k(x) \exp(\lambda_k t)$. Injecting this normal mode ansatz into (3.3) yields an eigenvalue problem

$$\lambda \hat{u} = J\hat{u}, \tag{3.4}$$

where $\lambda = \sigma + \mathrm{i}\omega$ is the eigenvalue and $\hat{u}$ its associated eigenvector. The linear stability of the fixed point is then dictated by the real part σ of the most unstable/least stable eigenvalue: the base flow is linearly unstable if $\sigma > 0$, otherwise it is linearly stable. Boundary conditions used to solve (3.4) are the same as those given in table 1, except at the inflow where a zero-velocity Dirichlet condition is now prescribed. It has to be noted however that because of the large number of degrees of freedom, solving the eigenproblem (3.3) using direct methods (i.e. QR or QZ algorithms) is hardly possible at the moment. Following Edwards *et al.* (1994) and Bagheri *et al.* (2009*a*), a time-stepper formulation of the problem is thus used. The leading eigenpairs of the linearized Navier–Stokes operator are then obtained based on the iterative Arnoldi algorithm (Arnoldi 1951) described by Loiseau *et al.* (2014) using a Krylov subspace of dimension $K = 250$ and a sampling period $\Delta T = 2.5$ in non-dimensional time units. For this selected set of parameters, each stability computation employs a wall-clock time of 15 to 20 h on 512–1024 cores. Thus, up to 20 000 CPU hours are needed to obtain one eigenvalue spectrum (without considering the CPU time for computing the base flow by continuation).

4. Results

4.1. *Primary bifurcation*

4.1.1. *Base flow*

As will be shown, the first bifurcation experienced by the flow results from an eigenvalue of the linearized Navier–Stokes operator crossing the neutral growth rate axis, which is characterized by a zero frequency. The corresponding eigenmode
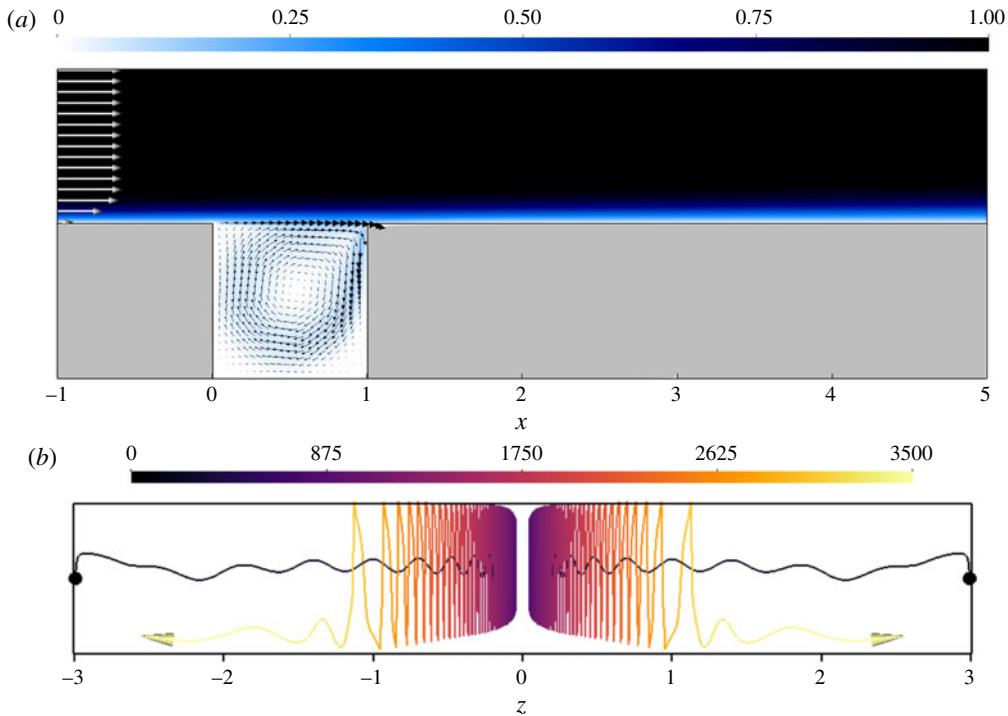
FIGURE 3. (Colour online) (*a*) Colour map of the velocity magnitude of the base flow at $Re = 3300$ in the symmetry $z = 0$ vertical plane. Only a subset of the whole computational domain is considered. (*b*) Visualization of the path lines of two particles located initially at $(x, y, z) = (0.5, -0.5, \pm 2.99)$. The incoming flow is directed toward the reader. The colour scale indicates the trajectory integration time.

thus experiences an exponential growth but does not exhibit periodic oscillation. Consequently, the popular selective frequency damping (Åkervik *et al.* 2006) cannot quench its development, and a continuation method similar to Theofilis & Colonius (2003) is thus used to compute linearly unstable base flows close to the first bifurcation threshold.

Figure 3 depicts some of the key features of the primary base flow. Though it is fully three-dimensional due to the spanwise end walls being taken into consideration, it can be seen that the flow within the central plane (given by $z = 0$) looks quite similar to its two-dimensional counterpart: see figure 3(*a*). Despite this apparent resemblance, the three-dimensionality of the flow within the cavity is clearly visible in figure 3(*b*) depicting some of the streamlines of the inner cavity flow. Fluid particles in the vicinity of the spanwise end walls are attracted toward the $z = 0$ plane along the central vortex. This spanwise flow results from the interaction between the swirling flow within the central plane and the zero-velocity condition prescribed at the spanwise end walls. Because of the friction along these end walls, the x- and y-velocity components are damped. However, due to the incompressibility of the flow, this deceleration of the (x, y) in-plane motion gives rise to a secondary flow which is directed along the z-axis as illustrated by the streamline visualizations. This secondary flow, from the spanwise end walls toward the central plane of the cavity,
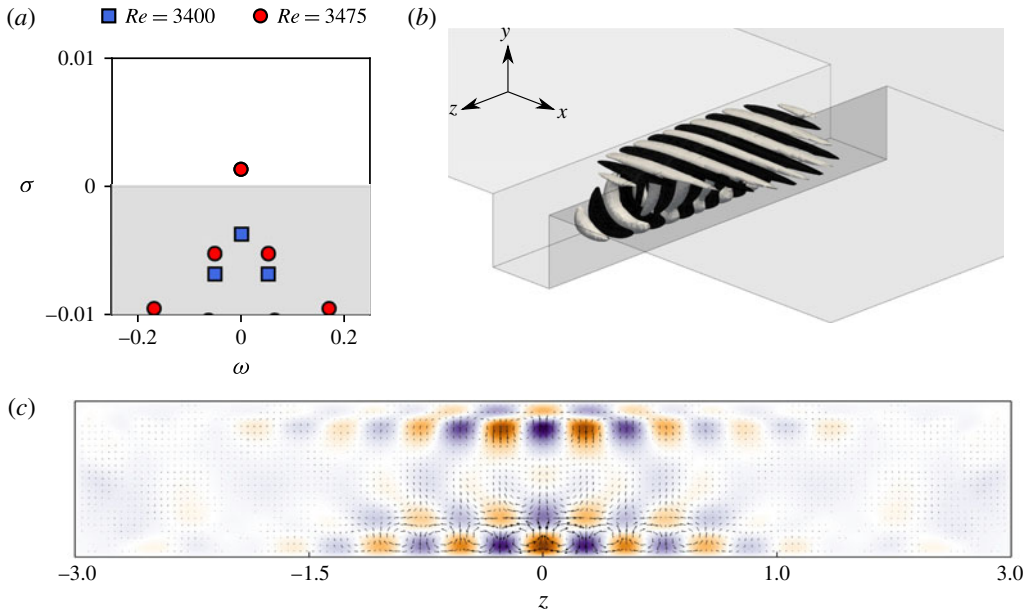
FIGURE 4. (Colour online) (*a*) Eigenspectra of the linearized Navier–Stokes operator for $Re = 3400$ (blue squares) and $Re = 3475$ (red circles). The shaded region corresponds to the stable part of the complex plane. (*b*) Spanwise velocity isocontours of the leading unstable mode at $Re = 3475$. (*c*) Motion induced by this mode in the $y = -0.5$ horizontal plane. The colour map depicts the amplitude of the out-of-plane (vertical) velocity component while the vectors show the in-plane motion.

occurs within the core of the primary vortex which experiences a solid-body-like rotation. Once it has reached the central plane, the fluid particles stay in its vicinity for a while before being expelled toward the end walls.

4.1.2. *Eigenspectra and eigenfunctions*

Figure 4(*a*) depicts the eigenspectra of the linearized Navier–Stokes operator at $Re = 3400$ and $Re = 3475$. All the eigenmodes are stable at $Re = 3400$ (blue squares). Increasing the Reynolds number, a real eigenvalue crosses the neutral axis becoming unstable (red dots). A linear interpolation gives a critical Reynolds number $Re_{C1} = 3450$. Spanwise velocity contours of the eigenvector corresponding to the leading eigenvalue are depicted in figure 4(*b*), while the motion induced in the $y = -0.5$ horizontal plane is highlighted in figure 4(*c*). It consists of a set of counter-rotating Taylor–Görtler-like vortices. Similar unstable structures also appear in the canonical lid-driven cavity flow (Albensoeder *et al.* 2001; Ramanan & Homsy 1994; Non *et al.* 2006; Chicheportiche *et al.* 2008; Theofilis *et al.* 2004; Feldman & Gelfgat 2010; Loiseau *et al.* 2016). Similar modes for the two-dimensional shear-driven cavity flow have been computed by Bres & Colonius (2008), Meseguer-Garrido *et al.* (2014), de Vicente *et al.* (2014) and observed experimentally by Faure *et al.* (2007, 2009), Douay *et al.* (2016*b*) and Douay, Lusseyran & Pastur (2016*a*). A Fourier decomposition of the mode in the spanwise direction indicates that the dominant wavelength is $\lambda_z = 0.515$, in
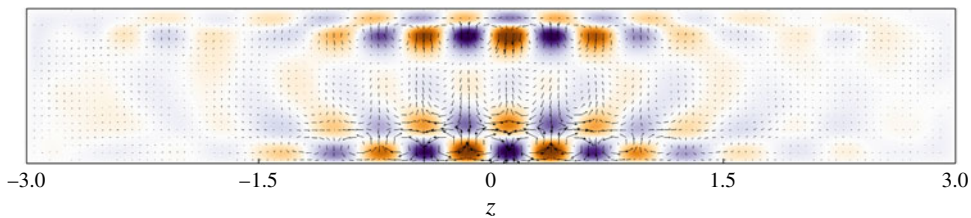
FIGURE 5. (Colour online) Motion induced by the least unstable mode in the $y = -0.5$ horizontal plane at $Re = 3475$. The colour map depicts the amplitude of the out-of-plane (vertical) velocity component while the vectors show the in-plane motion. Note that, contrary to the unstable mode, this one is characterized by a mirror antisymmetry.

good agreement with previous findings. Finally, it has to be noted that, on the eigenspectra depicted in figure 4(*a*), a second real eigenvalue is almost indiscernible from the leading unstable one, their growth rates differing by less than 1 %. The spatial distribution of the eigenvector associated with this eigenvalue is shown in figure 5. Comparing figures 4(*c*) and 5, these two eigenfunctions appear to be quite similar, both exhibiting the same spanwise wavenumber $\lambda_z \simeq 0.51$. However, while the eigenfunction associated with the most unstable eigenvalue exhibits a mirror symmetry, the one associated with the least unstable eigenvalue displays a mirror antisymmetry. Although this antisymmetric eigenmode is linearly unstable at the Reynolds numbers considered, it has never been observed in our direct numerical simulations. A similar observation has also been reported by Loiseau (2014) for three-dimensional lid-driven cavity flows. From a mathematical point of view, both of these two modes can be traced back to the same leading spanwise-periodic instability mode $\hat{\boldsymbol{u}}(x, y, \beta)$ of the two-dimensional shear-driven cavity. The mirror-symmetric mode would then asymptotically tend to

$$\lim_{S \to \infty} \boldsymbol{u}(x, y, z) = \hat{\boldsymbol{u}}(x, y) \cos(\beta z), \qquad (4.1)$$

where S is the spanwise extent of the cavity, while the mirror-antisymmetric mode would tend to

$$\lim_{S \to \infty} \boldsymbol{u}(x, y, z) = \hat{\boldsymbol{u}}(x, y) \sin(\beta z). \qquad (4.2)$$

It is unclear at the present time whether these two eigenvalues are non-degenerate eigenvalues or if they are the same degenerate eigenvalue with a multiplicity 2.

4.1.3. *Physical mechanism*

Following Albensoeder *et al.* (2001), the velocity field $\boldsymbol{u}$ of the leading eigenvector is decomposed as

$$\boldsymbol{u} = \boldsymbol{u}_{\parallel} + \boldsymbol{u}_{\perp}, \qquad (4.3)$$

where $\boldsymbol{u}_{\parallel}$ is everywhere parallel to the direction of the base flow velocity vectors, while $\boldsymbol{u}_{\perp}$ is its orthogonal complement. Using such a decomposition, the unstable eigenmode can be understood as the superposition of two structures: counter-rotating rolls ($\boldsymbol{u}_{\perp}$) and streaky structures ($\boldsymbol{u}_{\parallel}$) aligned with the flow. While the rolls account for 40 % of the perturbation's kinetic energy, the remaining 60 % is provided by the streaky structure. Introducing this decomposition into the Reynolds–Orr equation

I_1	I_2	I_3	I_4	D
0.009	0.197	0.039	0.032	-0.27

TABLE 2. Contribution of the different production terms I_i and the viscous dissipation D to the total kinetic energy budget of the unstable mode at $Re = 3500$.

governing the evolution of the perturbation's kinetic energy, the production term $P = -\int_V \boldsymbol{u} \cdot (\boldsymbol{u} \cdot \boldsymbol{\nabla})\boldsymbol{U}_b \, \mathrm{d}V$ can be decomposed into the following four terms:

$$I_1 = -\int_V \boldsymbol{u}_\perp \cdot (\boldsymbol{u}_\perp \cdot \boldsymbol{\nabla})\boldsymbol{U}_b \, \mathrm{d}V, \quad I_2 = -\int_V \boldsymbol{u}_\parallel \cdot (\boldsymbol{u}_\perp \cdot \boldsymbol{\nabla})\boldsymbol{U}_b \, \mathrm{d}V, \quad (4.4a,b)$$

$$I_3 = -\int_V \boldsymbol{u}_\perp \cdot (\boldsymbol{u}_\parallel \cdot \boldsymbol{\nabla})\boldsymbol{U}_b \, \mathrm{d}V, \quad I_4 = -\int_V \boldsymbol{u}_\parallel \cdot (\boldsymbol{u}_\parallel \cdot \boldsymbol{\nabla})\boldsymbol{U}_b \, \mathrm{d}V. \quad (4.5a,b)$$

A different physical mechanism is associated with each of these four contributions. For instance, the I_2 term is associated with the lift-up mechanism (Landahl 1980), consisting of the transport of the base flow shear by counter-rotating rolls $\boldsymbol{u}_\perp$, which induce streaky structures $\boldsymbol{u}_\parallel$, whereas the I_3 term is linked to the anti-lift-up mechanism, an energy amplification mechanism typically found in stable columnar vortices (Antkowiak & Brancher 2007). The sign of the different integrals I_i then indicates whether the associated physical mechanism acts to promote (positive) or quench (negative) the instability considered. The contributions of these different production terms to the total kinetic energy budget are summarized in table 2. This energy budget is dominated by the I_2 term, characterizing the transfer of energy between the base flow and the perturbation through the lift-up mechanism (Landahl 1980). Very similar energy budgets have been obtained for lid-driven cavity flows by Albensoeder *et al.* (2001) and Loiseau *et al.* (2016), pointing to an instability of centrifugal type.

4.1.4. *Nonlinear evolution*

Starting from the linearly unstable base flow at $Re = 3500$, a direct numerical simulation has been run until nonlinear saturation is reached in order to gain a better understanding of the saturation process of the instability and of the flow it is giving rise to. Figure 6 depicts the evolution of the flow's kinetic energy once an almost statistical steady state has been reached. Although the linear stability predicts a non-oscillatory instability, a surprising low-frequency ($\omega \approx 0.009$) and low-amplitude (std $\approx 2.5 \times 10^{-5}$) oscillation of the perturbation's energy can be observed. At the present time, it is not clear how this oscillation arises. Two different hypotheses can be formulated.

(i) The combination of the Krylov subspace's dimension and of the sampling period of the snapshots does not allow us to span a sufficiently large number of periods of this low-frequency oscillation for the Arnoldi algorithm to appropriately estimate its phase, and hence the imaginary part of the leading eigenvalue.

(ii) Assuming the linear eigenmode is indeed non-oscillatory, the low-frequency low-amplitude oscillation observed might arise from nonlinear interaction between this mode and the secondary low-energy spanwise flow induced by the existence of the spanwise end walls discussed earlier.
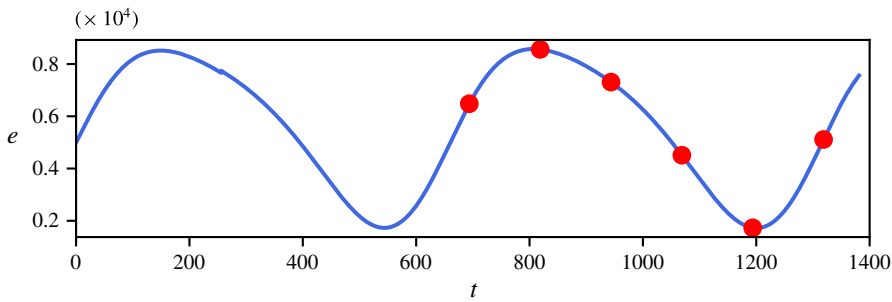
FIGURE 6. (Colour online) Evolution of the perturbation's kinetic energy as a function of time in the nonlinearly saturated regime at $Re = 3500$. Note that the vertical axis has been re-scaled by a factor 10^4. The red dots indicate the instants of time for which the corresponding helicity fields are depicted in figure 7.

The first hypothesis highlights potential limitations of the time-stepping approach when applied to linear stability analysis. Unfortunately, given our computational resources, it is not currently possible to increase significantly the dimension of the Krylov subspace and the associated sampling period in order to span several periods of this low-frequency oscillation. On the other hand, verifying the second hypothesis would rely on weakly nonlinear analyses (Sipp & Lebedev 2007) which are still very challenging for fully three-dimensional flow configurations and are beyond the scope of the present work. Figure 7 depicts the instantaneous spatial distribution of the helicity $h(x, t) = u(x, t) \cdot \omega(x, t)$ within the $y = -0.5$ horizontal plane at six different instants of time. As shown, the linearly unstable eigenmode reported in the previous section gives rise to five pairs of Taylor–Görtler-like vortices, the three central ones being largely more energetic than the outermost ones. These helicity maps also underline the strong swirling motion experienced by the fluid particles in the vicinity of the lateral walls and already outlined previously for the primary base flows: see figure 3(*b*). Looking at these different snapshots, it can finally be observed that the low-frequency oscillation observed in the flow's kinetic energy evolution depicted on figure 6 spatially corresponds to a small spanwise oscillation of these Taylor–Görtler-like vortices. Although a small change in the amplitude of the helicity is noticeable, one needs to recall that it occurs over several hundreds of convective time units. Moreover, it can be seen that these Taylor–Görtler vortices remain within the central part of the cavity delimited by $-1.5 \leqslant z \leqslant 1.5$.

4.2. *Secondary bifurcation*

4.2.1. *Base flow*

As shown in the previous section, the primary bifurcation gives rise to a flow characterized by a very low-frequency and low-amplitude oscillation of the central Taylor–Görtler-like vortices. Figure 8 depicts the instantaneous spatial distribution of the helicity $h(x)$ within the $y = -0.5$ horizontal plane at $Re = 3700$. It can be seen that the structure of the bifurcated flow is hardly modified when increasing the Reynolds number. A similar observation can be made regarding the frequency of the low-amplitude oscillation of the flow's kinetic energy (not shown). From a quantitative point of view, the total rate of change of the velocity field over $\Delta t = 2.5 \times 10^{-3}$ non-dimensional time units is of the order of 10^{-6}–10^{-7}. For linear
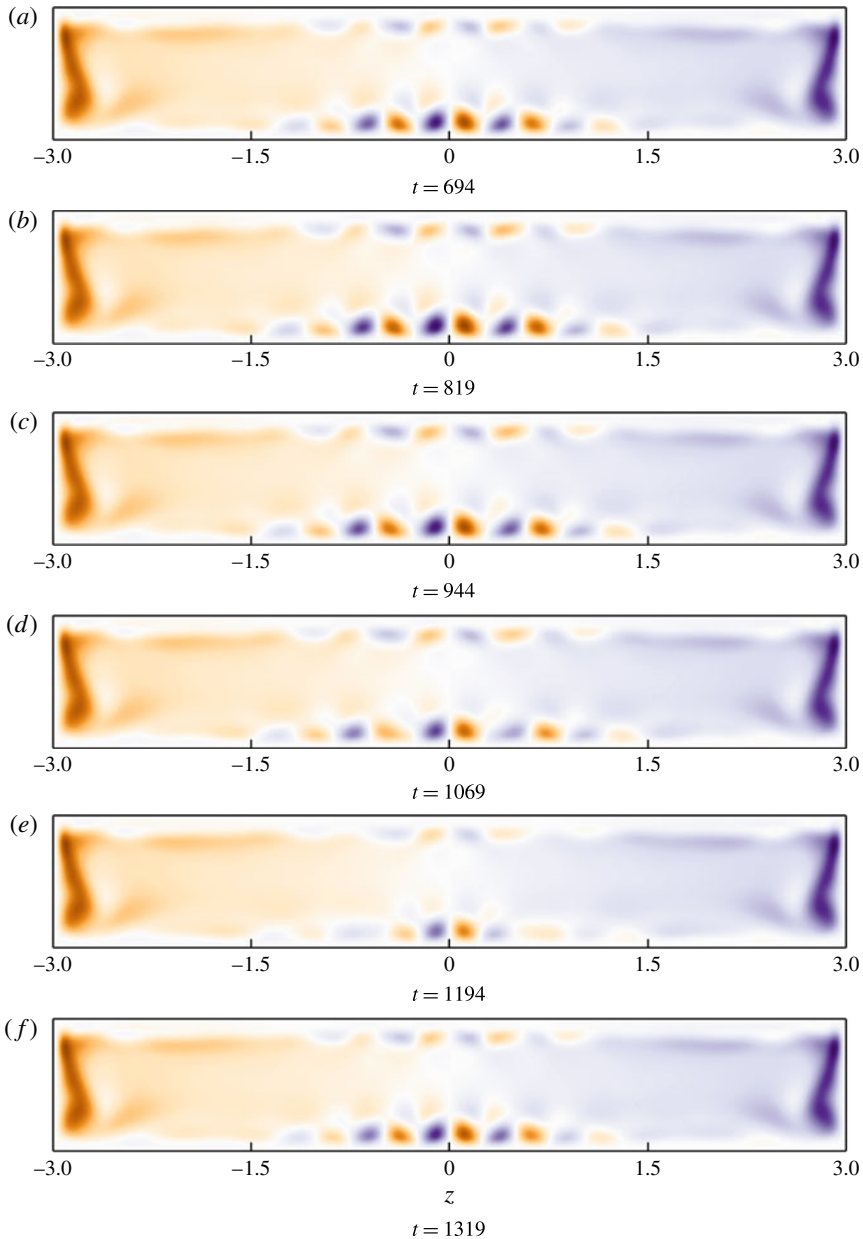
FIGURE 7. (Colour online) Snapshots of the instantaneous helicity field $\boldsymbol{h}(\boldsymbol{x}, t) = \boldsymbol{\omega}(\boldsymbol{x}, t) \cdot \boldsymbol{u}(\boldsymbol{x}, t)$ at the different instants of time highlighted in figure 6 ($Re = 3500$). The colour scale has been kept constant over the different figures.

stability analysis purposes, such a slowly evolving flow can thus be considered as being quasi-stationary and be used as a base flow. Since this small unsteadiness is moreover limited to the region $-1.5 \leqslant z \leqslant 1.5$, this quasi-static assumption is further strengthened *a posteriori* given that the spatial support of the second linearly unstable mode is almost entirely localized within the $\|z\| \geqslant 1.5$ region, as will be shown in the next section.
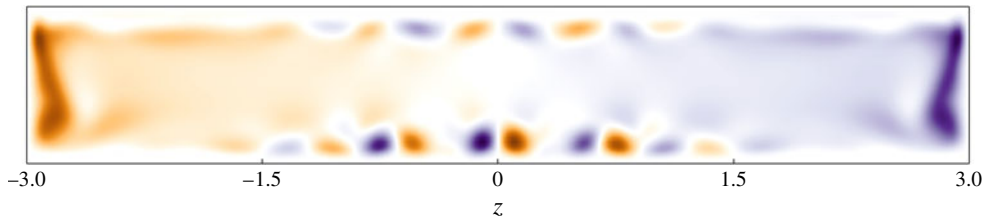
FIGURE 8. (Colour online) Helicity field of the bifurcated base flow within the $y = -0.5$ horizontal plane. The Reynolds number is set to $Re = 3700$.

4.2.2. *Eigenspectra and eigenfunctions*

Figure 9(*a*) depicts the eigenspectra of the linearized Navier–Stokes operator at $Re = 3600$ and $Re = 3800$. While for $Re = 3600$ all the modes are stable, it can be seen that at $Re = 3800$ two complex conjugate pairs of eigenvalues lie in the upper-half complex plane: $\lambda_2 = 0.0013 \pm i0.0496$ and $\lambda_3 = 0.0008 \pm i0.0272$, respectively. A linear interpolation gives a critical Reynolds number $Re_{C2} = 3730$ for the eigenvalue λ_2. The second bifurcation of the flow hence results from a pair of complex conjugate eigenvalues moving into the upper-half complex plane, i.e. an Andronov–Poincaré–Hopf bifurcation. Consequently, it leads the flow to exhibit self-sustained oscillations characterized by a circular frequency $\omega = \pm 0.0496$, i.e. four to five times larger than the low frequency of the low-amplitude oscillation of the base flow. The fact that a second unstable mode, λ_3, is observed at $Re = 3800$ indicates the existence of a second Hopf bifurcation, at a critical Reynolds number $Re_{C3} = 3770$ resulting from the eigenvalue λ_3 stepping into the upper-half complex plane.

Spanwise velocity contours of the eigenvector corresponding to the leading eigenvalue λ_2 are depicted in figure 9(*b*), while the motion induced in the $y = -0.5$ horizontal plane is depicted in figure 9(*c*). Note that the eigenvector associated with λ_3 is quite similar and is thus not shown for the sake of conciseness. Whereas the spatial support of the unstable eigenmode at the bifurcation point $Re_{C1} = 3430$ is mostly localized in the central part of the cavity ($\|z\| \leqslant 1.5$) (see figure 4), that depicted in figure 9 is essentially located in the outer part of the cavity given by $\|z\| \geqslant 1.5$. Although its spatial support lets us hypothesize that it is related to the existence of the spanwise end walls, it nonetheless takes the form of Taylor–Görtler-like vortices characterized by a spanwise wavelength $\lambda_z = 0.49$. As previously, this unstable eigenmode can be decomposed as $\boldsymbol{u} = \boldsymbol{u}_\parallel + \boldsymbol{u}_\perp$, with 61 % of the kinetic energy of the mode contained in the streaky structure $\boldsymbol{u}_\parallel$ while the rolls account for the remaining 39 %. Despite their different spatial locations, both the primary and secondary unstable eigenmodes hence appear to rely on the same underlying physical mechanisms. This is further confirmed by table 3, providing the contribution of the different productions terms I_i to the total kinetic energy budget. Once again, this energy budget is dominated by the I_2 term, hence implying that this secondary instability is also of centrifugal type. Finally, it is worth noting that the pair of complex conjugate eigenvalues now becoming unstable could already be foreseen at lower Reynolds numbers: see the least stable complex conjugate eigenvalues in the eigenspectrum shown in figure 4(*a*).

4.3. *Sensitivity analysis*

As explained in § 4.2.1, the stability analysis performed in the present section relies on the assumption that the time scale over which the secondary instability is evolving
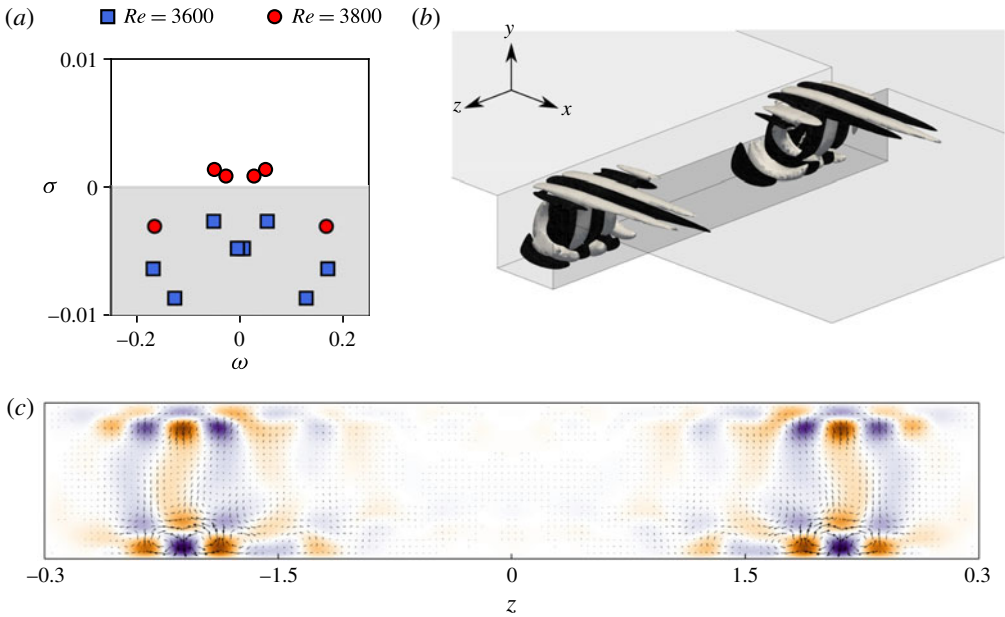
FIGURE 9. (Colour online) (*a*) Eigenspectra of the linearized Navier–Stokes operator for $Re = 3600$ (blue squares) and $Re = 3800$ (red circles). The shaded region corresponds to the stable part of the complex plane. (*b*) Spanwise velocity isocontours of the leading unstable mode at $Re = 3800$. (*c*) Motion induced by this mode in the $y = -0.5$ horizontal plane. The colour map depicts the amplitude of the out-of-plane (vertical) velocity component while the vectors show the in-plane motion.

I_1	I_2	I_3	I_4	D
0.0123	0.1782	0.0363	0.0225	-0.2463

TABLE 3. Contribution of the different production terms I_i and the viscous dissipation D to the total kinetic energy budget of the unstable mode at $Re = 3800$.

is significantly smaller than the period of the very low-frequency oscillation of the underlying base flow. Such an assumption is verified *a posteriori*, given that the frequency of the instability is four to five times larger than the low frequency of the base flow's oscillation. As shown in figure 9(*c*), the spatial support of the secondary mode moreover differs from that of the primary instability. Despite these key elements, one might nonetheless wonder how this secondary instability is influenced by the evolution of the flow within the central part of the cavity. Formally, one would need to perform a Floquet analysis, something which is beyond our current capabilities. Within our quasi-static assumption, such questioning can nonetheless be rephrased as: how sensitive is this secondary instability to base flow modifications? In order to answer this question, let us first introduce the adjoint Navier–Stokes equations

$$\left.\begin{aligned} \frac{\partial \boldsymbol{u}^{\dagger}}{\partial t} &= -\boldsymbol{\nabla}\boldsymbol{u}^{\dagger} \cdot \boldsymbol{U}_b + (\boldsymbol{\nabla}\boldsymbol{U}_b)^{\mathrm{T}} \cdot \boldsymbol{u}^{\dagger} - \boldsymbol{\nabla}p^{\dagger} + \frac{1}{Re}\nabla^2 \boldsymbol{u}^{\dagger}, \\ \boldsymbol{\nabla} \cdot \boldsymbol{u}^{\dagger} &= 0, \end{aligned}\right\} \tag{4.6}$$

where $\boldsymbol{u}^{\dagger}$ is the adjoint velocity field and $p^{\dagger}$ the adjoint pressure. As for the linearized Navier–Stokes equations, equation (4.6) can be recast as

$$\frac{\partial \boldsymbol{u}^{\dagger}}{\partial t} = \boldsymbol{J}^{\dagger} \boldsymbol{u}^{\dagger}, \tag{4.7}$$

where $\boldsymbol{J}^{\dagger}$ is the projection of the adjoint Jacobian matrix onto the divergence-free vector space. As this linear dynamical system is autonomous in time, the variable $\boldsymbol{u}^{\dagger}$ can once again be expanded into normal modes, such that one finally obtains the following eigenvalue problem:

$$\lambda^{\dagger} \hat{\boldsymbol{u}}^{\dagger} = \boldsymbol{J}^{\dagger} \hat{\boldsymbol{u}}^{\dagger}. \tag{4.8}$$

For each eigenpair $(\lambda_i, \hat{\boldsymbol{u}}_i)$ of the linearized Navier–Stokes operator, there exists an associated adjoint eigenpair $(\lambda_i^{\dagger}, \hat{\boldsymbol{u}}_i^{\dagger})$ such that

$$\lambda_i^{\dagger} = \lambda_i^{*} \quad \text{and} \quad \int_{\Omega} \hat{\boldsymbol{u}}_i \cdot \hat{\boldsymbol{u}}_j^{\dagger} \, \mathrm{d}\Omega = \delta_{ij}, \tag{4.9a,b}$$

where * denotes the complex conjugate operation. Given these direct and adjoint eigenpairs, it has been shown by Marquet, Sipp & Jacquin (2008) that the sensitivity of an eigenvalue λ of the linearized Navier–Stokes operator to modifications of the underlying base flow $\boldsymbol{U}_b$ is given by

$$\nabla_U \lambda = -(\nabla \hat{\boldsymbol{u}})^H \cdot \hat{\boldsymbol{u}}^{\dagger} + \nabla \hat{\boldsymbol{u}}^{\dagger} \cdot \hat{\boldsymbol{u}}^{*}, \tag{4.10}$$

where ^{H} denotes the transconjugate operation. The real part of (4.10) characterizes how and where the eigenvalue's growth rate σ is sensitive, while the imaginary part characterizes the sensitivity of the circular frequency ω to modification of the underlying base flow. For more details about the derivation of the adjoint equations, the sensitivity gradient and the boundary conditions to be applied, please refer to Barkley, Blackburn & Sherwin (2008), Blackburn, Barkley & Sherwin (2008), Marquet *et al.* (2008) or the recent review by Luchini & Bottaro (2014).

Figure 10 depicts the spanwise velocity field of the adjoint mode associated with the leading eigenmode depicted in figure 9 within the $y = -0.5$ horizontal plane, while the sensitivity of the corresponding growth rate within the same plane is shown in figure 11. Looking at these two figures, it is clear that the secondary instability is mostly sensitive in the vicinity of $z = \pm 2$, while modification within the central part of the cavity (i.e. where the very low-frequency oscillation of the base flow occurs) hardly influences it. Similar results have been obtained for the eigenmode associated with λ_3. Along with the very different spatial supports of the primary and secondary instability modes, these sensitivity results strongly justify *a posteriori* the validity of the frozen base flow assumption used in this section.

5. Discussion

5.1. *Comparisons with experiments*

The analyses reported in the previous sections have underlined how the flow can transition from steady state to the emergence of self-sustained periodic oscillations giving rise to a spanwise drift of the Taylor–Görtler-like vortices. Let us now compare the predictions of linear stability analyses and direct numerical simulations against
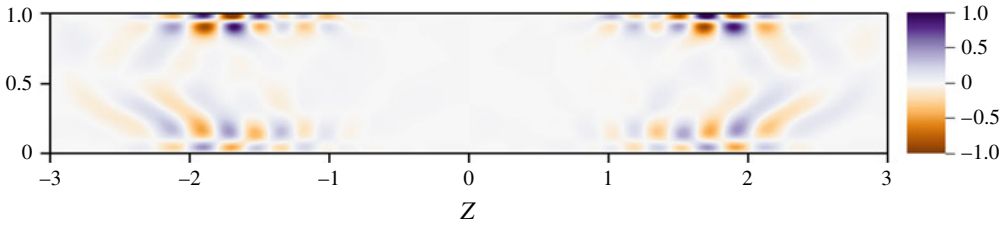
FIGURE 10. (Colour online) Spanwise velocity of the adjoint eigenmode $\hat{\boldsymbol{u}}^{\dagger}$ associated with the eigenvalue $\lambda = 0.001 \pm \text{i}0.049$ at $Re = 3800$ in the $y = -0.5$ horizontal plane.
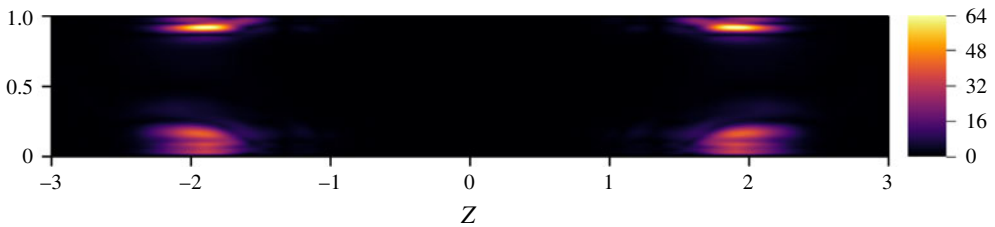

FIGURE 11. (Colour online) Sensitivity to base flow modification $\nabla_U \lambda$ of the eigenvector $\hat{\boldsymbol{u}}$ associated with the eigenvalue $\lambda = 0.001 \pm \text{i}0.049$ at $Re = 3800$ in the $y = -0.5$ horizontal plane. Only the magnitude of real part of $\nabla_U \lambda$ is shown, i.e. the sensitivity to base flow modification of the eigenvalue's growth rate.
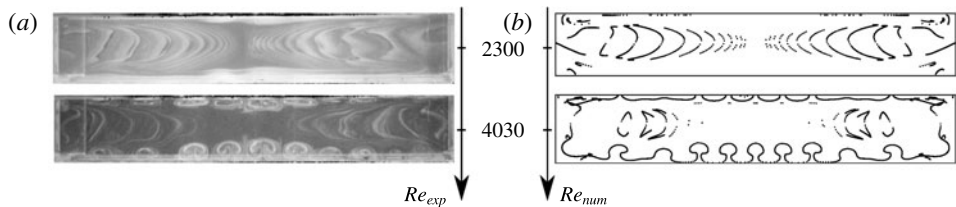

FIGURE 12. Experimental smoke visualization (*a*) (Faure *et al.* 2007) and numerically computed streamlines (*b*). The visualization technique enhances the detection of mushroom-shaped Taylor–Görtler-like vortical structures. Top views in the $y = 0.8$ plane.

observations obtained using the experimental set-up described in §2. Figure 12 depicts a visual comparison of the experimental smoke visualizations and the numerically computed streamlines within a horizontal plane cutting through the cavity at two different Reynolds numbers. It is clear that the flow patterns observed experimentally and numerically for the two Reynolds numbers considered are qualitatively similar. As the Reynolds number is increased from $Re = 2300$ up to $Re = 4030$, both the smoke and streamlines visualizations highlight the emergence of mushroom-like structures. These vortical structures are the Taylor–Görtler-like vortices resulting from the different centrifugal instabilities underlined in the previous sections.

Table 4 summarizes the critical Reynolds numbers, wavelengths and circular frequencies observed in our experimental work (see §2), in direct numerical simulations as well as in our linear stability analyses, while figure 13 provides a schematic representation of the evolution of the flow's morphology as the Reynolds number increases. As assessed from linear stability analyses, three different
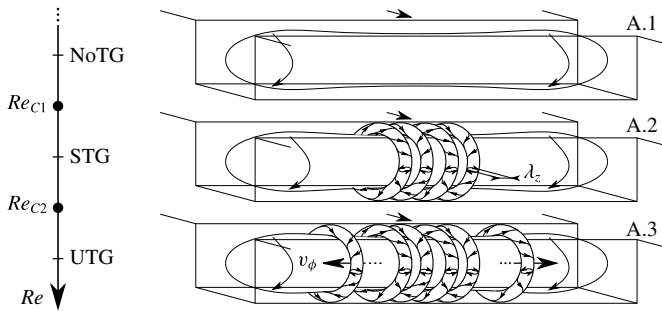
FIGURE 13. Sketch of the evolution of the morphology of the inner cavity's flow as a function of the Reynolds number. NoTG, STG and UTG stand for no Taylor–Görtler vortices, (quasi-) stationary Taylor–Görtler vortices and unsteady Taylor–Görtler vortices, respectively.

	Re_{C1}	Re_{C2}	λ_z	ω
Experimental	$\approx 3370 \pm 84$	$\approx 3750 \pm 94$	$0.53L$	0.035
DNS	3450	3730	$0.52L$	0.0343 $(Re = 3900)$
GLSA	3450	$3730 - 3770 (Re_{C3})$	$0.49L$	$0.049 - 0.027$ (ω_3)

TABLE 4. Summary of the critical Reynolds numbers, spanwise wavelength and circular frequencies observed experimentally, and predicted by linear stability analyses. DNS and GLSA stand for direct numerical simulation and global linear stability analysis, respectively.

flow regimes have been observed. The first one (figure 13a) is a stationary flow characterized by the absence of Taylor–Görtler vortices and sharing strong similarities with its two-dimensional counterpart. The second flow regime sees the emergence of Taylor–Görtler-like (TGL) vortices localized in the central part of the cavity. Although linear stability analyses predict a stationary flow, direct numerical simulations have revealed that these TGL vortices experience a very low-amplitude and low-frequency oscillation. Such oscillations are extremely difficult to observe owing to their small amplitude and the long time scale over which they take place. Nonetheless, the critical Reynolds number predicted by stability analysis is in extremely good agreement with both direct numerical simulations and experimental observations (only 2 % difference), as is the dominant wavelength of this vortical flow structure. On top of these quasi-stationary TGL vortices, travelling waves are observed in the third flow regime investigated due to the appearance of additional sets of linearly unstable TGL vortices now located in the vicinity of the spanwise end walls. Figure 14 depicts experimental and numerical spatio-temporal diagrams taken along the line $(x, y) = (0.1, 0.8)$ for $Re = 3900$. These diagrams once again highlight the good agreement obtained between the experimental and numerical flow patterns. In both configurations, the central region of the cavity, given by $\|z/D\| < 1$, is mostly dominated by quasi-steady Taylor–Görtler-like vortices characterized by a spanwise wavelength $\lambda_z \simeq 0.5$. On the other hand, the flow pattern in the outer parts of the cavity, given by $\|z/D\| > 1.5$, is dominated by a right- or left-travelling wave resulting from the instability reported in § 4.1.2. Physically, this travelling wave corresponds to a spanwise drift of the TGL vortices due to the existence of the secondary flow discussed in § 4.1.1 and already
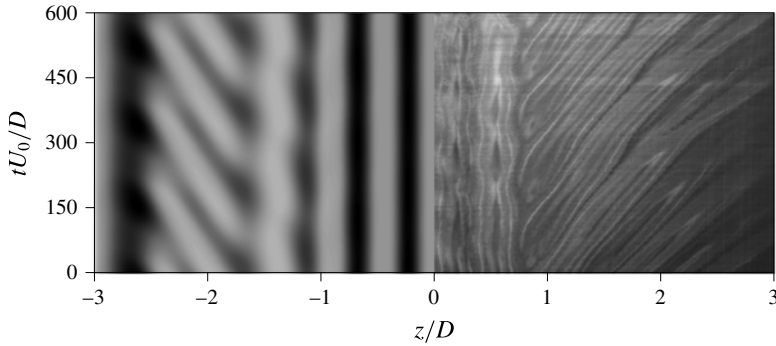
FIGURE 14. Numerical and experimental space–time diagrams of the pattern dynamics at $Re = 3900$ along the line $(x, y) = (0.1, 0.8)$. Streamwise velocity for DNS on the left, experimental smoke visualization on the right. The latter has been rectified using the constant asymmetrical drift velocity obtained for $Re_{C1} \leqslant Re \leqslant Re_{C2}$.

investigated experimentally by Faure *et al.* (2007), Faure *et al.* (2009) Douay (2014) and Douay *et al.* (2016b). As for the primary bifurcation, the critical experimental and theoretical critical Reynolds numbers differ by less than 1%. It has to be noted finally that some small discrepancies exist regarding the oscillation frequency of the lateral TGL vortices. This difference very likely results from small limitations of the experimental set-up highlighted in §2, namely the existence of a small non-vanishing spanwise component of the incoming flow introducing a systematic bias in the flow direction. Another source of error might reside in the quasi-static assumption made for the secondary base flow. Overcoming this limitation, however, requires the use of Floquet analysis, which is beyond our present capabilities.

5.2. *Influence of the aspect ratio*

The results presented so far have been obtained in the case of a relatively large-span square cavity of aspect ratio $L:D:S = 1:1:6$, recovering two successive bifurcations leading the flow to transition. Nonetheless, it is not clear yet whether the scenario observed herein might be extended to the flow in open cavities of different aspect ratios. Previous experimental works on square cavities ($L/D = 1$, see Faure *et al.* 2009) have shown how the spatial support of the flow instabilities changes drastically when the span to depth ratio, S/D, is decreased to values lower than 3. In these short-span cavities, isolated pairs of vortices are recovered instead of the spanwise rows of centrifugal vortices generally observed for large-span cavities, indicating that the strong spanwise flow induced by the presence of two neighbouring lateral walls may prevent the generation of the centrifugal vortices. However, for cavities having a sufficiently large-span size ($S/D \geqslant 3$), no abrupt change of the main features of the bifurcated flow is observed, the instability modes keeping a very similar shape when S/D is increased. In the limit of an infinitely large cavity, a spanwise-homogeneous open cavity flow is obtained, which has been studied numerically by Citro *et al.* (2015a) for the case $L/D = 1$. These authors have shown that the flow undergoes the first bifurcation at a critical Reynolds number of 1370, the most unstable mode being steady, localized inside the cavity and three-dimensional with spanwise wavelength of approximately 0.47 cavity depths. A structural sensitivity analysis provided by the same authors indicates that, for the considered infinite-span square cavity, the

mechanism of generation of the primary unstable mode is completely driven by the recirculating flow inside the cavity. Thus, the primary instability mechanism characterizing an infinite-span square cavity flow appears qualitatively similar to that recovered herein for a large-span cavity, although the critical Reynolds number as well as the dominating wavelengths and shape of the vortical structures are different to those obtained in the present work.

Concerning the case of large-span cavities, Douay (2014) has experimentally investigated their flow dynamics for different aspect ratios. In particular, it has been observed that, for a span ratio $S/D = 6$, for any L/D ratio, the frequency of the primary bifurcation remains rather low (the associated Strouhal number, St, being of order 10^{-3}), being associated with quasi-steady spanwise-alternated Taylor–Görtler modes. For $S/D = 12$, two different behaviours have been recovered depending on the aspect ratio L/D. For $L/D < 1.3$, the primary modes pertain to the previously mentioned quasi-steady family, whereas for $L/D \geqslant 1.4$, the Strouhal number abruptly increases by one order of magnitude, being associated with propagating modes similar to those previously identified by Bres & Colonius (2008), Faure *et al.* (2009), Meseguer-Garrido *et al.* (2014). This indicates that not only the span ratio but also the length ratio may be a critical parameter for the destabilization of open cavity flows, as previously observed in several experimental studies (Gharib & Roshko 1987). This is further confirmed by the results recently provided by Liu *et al.* (2016), who performed a global stability analysis on the flow over a long cavity of aspect ratio $L\!:\!D\!:\!S = 6\!:\!1\!:\!2$. For $Re < 1050$, the leading (although stable) mode is steady and driven by a centrifugal mechanism. This mode is rapidly overtaken by a shear-layer-driven travelling eigenmode, characterized by a relatively high frequency ($St \approx 0.23$), which becomes unstable at $Re \approx 1080$, leading to laminar–turbulent transition. Also for this long cavity, the typical structure of the centrifugal steady mode is reminiscent of the pattern found in previous investigations of spanwise-homogeneous cavity flows (Bres & Colonius 2008). However, when a spanwise-homogeneous long cavity with $L/D = 6$ is considered (see Sun *et al.* 2014) no steady modes are recovered in the flow dynamics. This suggests that shear-layer modes may be dominant for long cavities, whereas steady centrifugal ones would prevail in short ones, although modifying the span of the cavity might induce a further change in the flow dynamics. A spanwise-homogeneous approximation might, in some particular cases, succeed at detecting (although qualitatively) the main instability mechanisms driving the flow, but will fail at predicting the critical thresholds for transition as well as the dominant frequencies and wavelengths. This confirms the need of performing global stability analyses for accurately investigating the dynamics of such three-dimensional flows for different aspect ratios.

6. Conclusion

The transition scenario of an incompressible shear-driven cavity flow has been investigated by the joint application of experimental observations, direct numerical simulations and linear stability analyses. Based on the good agreement obtained using these different approaches, a clear scenario is here proposed to explain the transition to unsteadiness. This scenario relies on the occurrence of two successive bifurcations. The first one, happening at a critical Reynolds number $Re_{C1} = 3430$, is associated with the emergence of (quasi-)steady Taylor–Görtler vortices. Analysis of the different production terms has revealed the centrifugal nature of the instability, in agreement with previous studies on the two-dimensional shear-driven and lid-driven

cavities (Albensoeder *et al.* 2001). Further increasing the Reynolds number up to $Re_{C2} \simeq 3730$ eventually causes a second bifurcation to occur. This second bifurcation is an Andronov–Poincaré–Hopf bifurcation. The flow thus transitions from its quasi-stationary bifurcated state and exhibits self-sustained periodic oscillations. Though a kinetic energy analysis has revealed that the underlying instability is also of centrifugal type, it has to be noted that it nonetheless differs quite significantly from the primary instability. Indeed, while the first instability occurring in the flow is exclusively related to the primary vortex core, the second instability reported in the present work is clearly related to the interplay between the primary vortex core and the existence of the spanwise end walls of the cavity. As a result of this secondary instability, the periodic oscillations of the flow are characterized by a spanwise drift of the vortical structures toward the end walls very likely induced by the existence of the spanwise secondary flow. Although it has been hypothesized in the past (Faure *et al.* 2009; Douay 2014) that this drift might result from a global instability of the flow, it is the first time to our knowledge that it has been properly demonstrated by means of fully three-dimensional stability analyses.

Despite linear stability analysis having proved helpful since the early 1900s to gain a better understanding of the fundamental physical mechanisms on which transition to turbulence relies, it fully explains the transition scenario only for a limited number of flow configurations, e.g. Rayleigh–Bénard or the two-dimensional cylinder flow, for instance. Given its wall-bounded nature, it is thus remarkable that linear stability analyses can fully characterize the first two bifurcations taking place in the fully three-dimensional shear-driven cavity flow. Building on this success, our joint experimental and numerical efforts are thus currently aiming at the proper characterization of the second and third bifurcations by means of Floquet analyses. It has to be noted finally that the transition scenario presented in this work is quite different from the one originally proposed by Liu *et al.* (2016) for a similar flow configuration and relying on the emergence of Rossiter-like instability modes. This apparent contradiction, however, results from the significantly different geometry of the cavities considered in these two works. Researchers and engineers willing to pursue this work are thus strongly encouraged to perform parametric studies in order to fully elucidate the influence of the cavity's dimensions on these transition scenarios.

Acknowledgements

REFERENCES

ÅKERVIK, E., BRANDT, L., HENNINGSON, D. S., HOEPFFNER, J., MARXEN, O. & SCHLATTER, P. 2006 Steady solutions of the navier-stokes equations by selective frequency damping. *Phys. Fluids* **18** (6), 068102.

ALBENSOEDER, S. & KUHLMANN, H. C. 2006 Nonlinear three-dimensional flow in the lid-driven square cavity. *J. Fluid Mech.* **569**, 465–480.

ALBENSOEDER, S., KUHLMANN, H. C. & RATH, H. J. 2001 Three-dimensional centrifugal-flow instabilities in the lid-driven cavity problem. *Phys. Fluids* **13**, 121–135.

ANTKOWIAK, A. & BRANCHER, P. 2007 On vortex rings around vortices: an optimal mechanism. *J. Fluid Mech.* **578**, 295–304.

ARNOLDI, W. E. 1951 The principle of minimized iterations in the solution of the matrix eigenvalue problem. *Q. Appl. Maths* **9** (1), 17–29.

BAGHERI, S., ÅKERVIK, E., BRANDT, L. & HENNINGSON, D. S. 2009*a* Matrix-free methods for the stability and control of boundary layers. *AIAA J.* **47** (5), 1057–1068.

BAGHERI, S., SCHLATTER, P., SCHMID, P. J. & HENNINGSON, D. S. 2009*b* Global stability of a jet in crossflow. *J. Fluid Mech.* **624**, 33–44.

BARBAGALLO, A., SIPP, D. & SCHMID, P. J. 2009 Closed-loop control of an open cavity flow using reduced-order models. *J. Fluid Mech.* **641**, 1–50.

BARKLEY, D., BLACKBURN, H. M. & SHERWIN, S. J. 2008 Direct optimal growth analysis for timesteppers. *Intl J. Numer. Meth. Fluids* **57** (9), 1435–1458.

BARKLEY, D., GOMES, G. M. & HENDERSON, R. D. 2002 Three-dimensional instability in flow over a backward-facing step. *J. Fluid Mech.* **473**, 167–190.

BASLEY, J., PASTUR, L. R., DELPRAT, N. & LUSSEYRAN, F. 2013 Space-time aspects of a three-dimensional multi-modulated open cavity flow. *Phys. Fluids* **25**, 064105.

BASLEY, J., PASTUR, L. R., LUSSEYRAN, F., SORIA, J. & DELPRAT, N. 2014 On the modulating effect of three-dimensional instabilities in open cavity flows. *J. Fluid Mech.* **759**, 546–578.

BEAUDOIN, J.-F., CADOT, O., AIDER, J.-L. & WESFREID, J. E. 2004 Three-dimensional stationary flow over a backward-facing step. *Eur. J. Mech.* (*B/Fluids*) **23**, 147–155.

BLACKBURN, H. M., BARKLEY, D. & SHERWIN, S. J. 2008 Convective instability and transient growth in flow over a backward-facing step. *J. Fluid Mech.* **603**, 271–304.

BRES, G. & COLONIUS, T. 2008 Three-dimensional instabilities in compressible flow over open cavities. *J. Fluid Mech.* **599**, 309–339.

CHERUBINI, S., ROBINET, J.-CH., DE PALMA, P. & ALIZARD, F. 2010 The onset of three-dimensional centrifugal global modes and their nonlinear development in a recirculating flow over a flat surface. *Phys. Fluids* **22** (11), 114102.

CHICHEPORTICHE, J., MERLE, X., GLOERFELT, X. & ROBINET, J.-CH. 2008 Direct numerical simulation and global stability analysis of three-dimensional instabilities in a lid-driven cavity. *C. R. Mech.* **336** (7), 586–591.

CITRO, V., GIANNETTI, F., BRANDT, L. & P., LUCHINI 2015*a* Linear three-dimensional global and asymptotic stability analysis of incompressible open cavity flow. *J. Fluid Mech.* **768**, 113–140.

CITRO, V, GIANNETTI, F, LUCHINI, P & AUTERI, F 2015*b* Global stability and sensitivity analysis of boundary-layer flows past a hemispherical roughness element. *Phys. Fluids* **27** (8), 084110.

CONWAY, S. L., SHINBROT, T. & GLASSER, B. J. 2004 A Taylor vortex analogy in granular flows. *Nature* **431** (7007), 433–437.

DENHAM, MK & PATRICK, MA 1974 Laminar flow over a downstream-facing step in a two-dimensional flow channel. *Trans. Inst. Chem. Engrs* **52** (4), 361–367.

DING, Y. & KAWAHARA, M. 1998 Linear stability of incompressible fluid flow in a cavity using finite element method. *Intl J. Numer. Meth. Fluids* **27**, 139–157.

DOUAY, C. 2014 Etude expérimentale paramétrique des propriétés et transitions de l'écoulement intra-cavitaire en cavité ouverte et contrôle de l'écoulement. PhD thesis, Université Pierre et Marie Curie.

DOUAY, C. L., LUSSEYRAN, F. & PASTUR, L. R. 2016*a* The onset of centrifugal instability in an open cavity flow. *Fluid Dyn. Res.* **48** (6), 061410.

DOUAY, C. L., PASTUR, L. R. & LUSSEYRAN, F. 2016*b* Centrifugal instabilities in an experimental open cavity flow. *J. Fluid Mech.* **788**, 670–694.

EDWARDS, W. S., TUCKERMAN, L. S., FRIESNER, R. A. & SORENSEN, D. C. 1994 Krylov methods for the incompressible Navier–Stokes equations. *J. Comput. Phys.* **110**, 82–102.

FAURE, M. T., PASTUR, L., LUSSEYRAN, F., FRAIGNEAU, Y. & BISH, D. 2009 Three-dimensional centrifugal instabilities development inside a parallelepipedic open cavity of various shape. *Exp. Fluids* **47**, 395–410.

FAURE, T., ADRIANOS, P., LUSSEYRAN, F. & PASTUR, L. 2007 Visualizations of the flow inside an open cavity at medium range Reynolds numbers. *Exp. Fluids* **42**, 169–184.

FELDMAN, Y. & GELFGAT, A. YU. 2010 Oscillatory instability of a three-dimensional lid-driven flow in a cube. *Phys. Fluids* **22** (9), 093602.

FISCHER, P., KRUSE, J., MULLEN, J., TUFO, H., LOTTES, J. & KERKEMEIER, S. 2008 Open source spectral element CFD solver. https://nek5000.mcs.anl.gov/index.php/MainPage.

GHARIB, M. & ROSHKO, A. 1987 The effect of flow oscillations on cavity drag. *J. Fluid Mech.* **177**, 501–530.

GÓMEZ, F., GÓMEZ, R. & THEOFILIS, V. 2014 On three-dimensional global linear instability analysis of flows with standard aerodynamics codes. *Aerosp. Sci. Technol.* **32** (1), 223–234.

GUERMOND, J.-L., MIGEON, C., PINEAU, G. & QUARTAPELLE, L. 2002 Start-up flows in a three-dimensional rectangular driven cavity of aspect ratio $1:1:2$ at $Re = 1000$. *J. Fluid Mech.* **450**, 169–199.

GURNETT, D. A., PERSOON, A. M., KURTH, W. S., GROENE, J. B., AVERKAMP, T. F., DOUGHERTY, M. K. & SOUTHWOOD, D. J. 2007 The variable rotation period of the inner region of Saturn's plasma disk. *Science* **316**, 442–445.

ILAK, M., SCHLATTER, P., BAGHERI, S. & HENNINGSON, D. S. 2012 Bifurcation and stability analysis of a jet in cross-flow: onset of global instability at a low velocity ratio. *J. Fluid Mech.* **686**, 94–121.

KUHLMANN, H. C. & ALBENSOEDER, S. 2014 Stability of the steady three-dimensional lid-driven flow in a cube and the supercritical flow dynamics. *Phys. Fluids* **26** (2), 024104.

LANDAHL, M. T. 1980 A note on an algebraic instability of inviscid parallel shear flows. *J. Fluid Mech.* **98**, 243–251.

LIU, Q., GÓMEZ, F. & THEOFILIS, V. 2016 Linear instability analysis of low-incompressible flow over a long rectangular finite-span open cavity. *J. Fluid Mech.* **799**, R2.

LOISEAU, J.-CH. 2014 Dynamics and global stability of three-dimensional flows. PhD thesis, Arts & Métiers ParisTech.

LOISEAU, J.-CH., ROBINET, J.-CH., CHERUBINI, S. & LERICHE, E. 2014 Investigation of the roughness-induced transition: global stability analyses and direct numerical simulations. *J. Fluid Mech.* **760**, 175–211.

LOISEAU, J.-CH., ROBINET, J.-CH. & LERICHE, E. 2016 Intermittency and transition to chaos in the cubical lid-driven cavity flow. *Fluid Dyn. Res.* **48** (6), 061421.

LUCHINI, P. & BOTTARO, A. 2014 Adjoint equations in stability analysis. *Annu. Rev. Fluid Mech.* **46** (1), 493–517.

MARQUET, O., SIPP, D. & JACQUIN, L. 2008 Sensitivity analysis and passive control of cylinder flow. *J. Fluid Mech.* **615**, 221–252.

MESEGUER-GARRIDO, F., DE VICENTE, J., VALERO, E. & THEOFILIS, V. 2014 On linear instability mechanisms in incompressible open cavity flow. *J. Fluid Mech.* **752**, 219–236.

MOLEMAKER, M. J., MCWILLIAMS, J. C. & YAVNEH, I. 2001 Instability and equilibration of centrifugally stable stratified Taylor–Couette flow. *Phys. Rev. Lett.* **86**, 5270.

NON, E., PIERRE, R. & GERVAIS, J.-J. 2006 Linear stability of the three-dimensional lid-driven cavity. *Phys. Fluids* **18** (8), 084103.

PEPLINSKI, A., SCHLATTER, P. & HENNINGSON, D. S. 2015 Global stability and optimal perturbation for a jet in cross-flow. *Eur. J. Mech.* (B*/Fluids*) **49**, 438–447.

RAMANAN, N. & HOMSY, G. M. 1994 Linear stability of lid-driven cavity flow. *Phys. Fluids* **6**, 2690–2701.

ROSSITER, J. E. 1964 Wind tunnel experiments on the flow over rectangular cavities at subsonic and transonic speeds. *Tech. Rep.*, Royal Aircraft Establishment, Farnborough. Ministry of Aviation.

ROWLEY, C. W., COLONIUS, T. & BASU, A. J. 2002 On self-sustained oscillations in two-dimensional compressible flow over rectangular cavities. *J. Fluid Mech.* **455**, 315–346.

SCHMID, P. J. 2010 Dynamic mode decomposition of numerical and experimental data. *J. Fluid Mech.* **656**, 5–28.

SIPP, D. & LEBEDEV, A. 2007 Global stability of base and mean flows: a general approach and its applications to cylinder and open cavity flows. *J. Fluid Mech.* **593**, 333–358.

SIPP, D., MARQUET, O., MELIGA, P. & BARBAGALLO, A. 2010 Dynamics and control of global instabilities in open-flows: a linearized approach. *Appl. Mech. Rev.* **63** (3), 030801.

SISAN, D. R., MUJICA, N., TILLOTSON, W. A., HUANG, Y.-M., DORLAND, W., HASSAM, A. B., ANTONSEN, T. M. & LATHROP, D. P. 2004 Experimental observation and characterization of the magnetorotational instability. *Phys. Rev. Lett.* **93**, 114502.

SUN, Y., NAIR, A. G., TAIRA, K., CATTAFESTA, L. N., BRES, G. A. & UKEILEY, L. S. 2014 Numerical simulations of subsonic and transonic open-cavity flows. *AIAA Paper* 3092.

THEOFILIS, V. & COLONIUS, T. 2003 An algorithm for the recovery of 2-D and 3-D BiGlobal instabilities of compressible flow over 2-D open cavities. *AIAA Paper* 2003-4143.

THEOFILIS, V., DUCK, P. W. & OWEN, J. 2004 Viscous linear stability analysis of rectangular duct and cavity flows. *J. Fluid Mech.* **505**, 249–286.

THEOFILIS, V., HEIN, S. & DALLMANN, U. 2000 On the origin of unsteadiness and three-dimensionality in a laminar separation bubble. *Phil. Trans. R. Lond.* A **358**, 3229–3246.

DE VICENTE, J., BASLEY, J., MESEGUER-GARRIDO, F., SORIA, J. & THEOFILIS, V. 2014 Three-dimensional instabilities over a rectangular open cavity: from linear stability analysis to experimentation. *J. Fluid Mech.* **748**, 219–236.

YAMOUNI, S., SIPP, D. & JACQUIN, L. 2013 Interaction between feedback aeroacoustic and acoustic resonance mechanisms in a cavity flow: a global stability analysis. *J. Fluid Mech.* **717**, 134–165.